025921-29-T

Edge-based finite elements and vector ABCs applied to 3D scattering

A. Chatterjee, J. M. Jin and J. L. Volakis

National Aeronautics and Space Administration
Ames Research Center
Moffett Field CA 94035

Pacific Missile Test Center
Pt. Mugu CA
93042-5000

May 1992

THE UNIVERSITY OF MICHIGAN
Radiation Laboratory
Department of Electrical Engineering
and Computer Science
Ann Arbor, Michigan 48109-2122
USA

(NASA-CR-190352) EDGE-BASED FINITE ELEMENTS AND VECTOR ABCs APPLIED TO 3D SCATTERING Technical Report, Feb. - Sep. 1992 (Michigan Univ.) 20 p

N92-26132

Unclas
G3/32 0091534

025921-29-T

TECHNICAL REPORT

for NASA Grant NAG-2-541

NASA Technical Monitor: Alex Woo

Grant Title:	Development of 3D Electromagnetic Modeling Tools for Airborne Vehicles
Report Title:	Edge-Based Finite Elements and Vector ABCs Applied to 3D Scattering
Institution:	Radiation Laboratory Department of Electrical Engineering and Computer Science The University of Michigan Ann Arbor MI 48109-2122
Period Covered:	Feb. 1992 – Sept. 1992
Report Authors:	A. Chatterjee, J.M. Jin and J.L. Volakis
Principal Investigator:	John L. Volakis Telephone: (313) 764-0500

Edge-based finite elements and vector ABCs applied to 3D scattering

A. Chatterjee, J. M. Jin and J. L. Volakis
Radiation Laboratory
Department of Electrical Engineering
and Computer Science
University of Michigan
Ann Arbor MI 48109-2122

Abstract

An edge-based finite element formulation with vector absorbing boundary conditions is presented for scattering by composite structures having boundaries satisfying impedance and/or transition conditions. Remarkably accurate results are obtained by placing the mesh a small fraction of a wavelength away from the scatterer.

1 Introduction

Of generic interest in electromagnetic scattering is the modelling of composite configurations comprised of metallic and non-metallic sections. In the case of man-made structures, abrupt material discontinuities and metallic corners are also encountered along with resistive sheets and thin ferrite coatings intended for controlling the scatterer's radar cross-section (RCS). Differential equation methods, especially the finite element method (FEM), with its capability of handling arbitrary geometries and its versatility in modelling inhomogeneities and material discontinuities has been a viable solution approach for bounded domain problems. However, for unbounded problems as is the case with electromagnetic scattering, the solution is more involved since the finite element mesh needs to be truncated artificially at some distance from the object with a suitable boundary condition. These boundary conditions can be either global or local. Global boundary conditions are exact but lead to fully populated submatrices thus spoiling the sparse, banded structure of the finite element system. In contrast, local conditions such as the absorbing boundary conditions(ABCs), are approximate but have the important advantage of retaining the sparsity of the matrix system. ABCs are essentially differential equations enforced at the mesh truncation boundary and are chosen to suppress all non-physical reflections from that boundary, thus ensuring the outgoing nature of the waves.

A variety of ABCs have been derived and widely employed in FEM solutions of open region two-dimensional scattering problems. However, the method's implementation and performance for scattering by three dimensional geometries using edge-based finite elements has not received similar attention. The only three-dimensional implementations of the FEM for scattering has been a hybrid solution combined with the boundary element method (BEM)[1,2] and a node-based formulation combined with ABCs[3]. The boundary element method, though exact, is equivalent to employing a global boundary condition for terminating the mesh and consequently leads to a full matrix, restricting the method's utility to small geometries. For large-scale three-dimensional applications, it is necessary to employ an ABC for terminating the mesh to retain the $O(N)$ storage requirement, characteristic of the finite element method. However, the use of traditional node-based elements for solving electromagnetic problems complicates the enforcement of the required boundary conditions at material discontinuities and impedance boundaries or resistive transitions. Moreover, the inherent singularities of the electromagnetic fields at metallic corners limits their use altogether.

To avoid these difficulties, we consider an implementation of the FEM using vector basis functions whose degrees of freedom are associated with the fields along the six edges of a tetrahedron. In contrast to the traditional node-based elements, edge elements can treat geometries with sharp edges and are divergenceless. Moreover, they exhibit tangential continuity and normal discontinuity across inter-element boundaries and material discontinuities, thus making them ideal for representing electromagnetic fields. They

do, however, lead to a higher number of unknowns but this is balanced by the greater sparsity of the resulting finite element matrix. Thus the computation time required to solve such a system iteratively, with a given degree of accuracy, is less than the traditional node-based approach[4]. Our implementation is further coupled with a mesh termination scheme based on the vector ABCs derived in [5]. In contrast to the implementation proposed in [6], the one presented here preserves the symmetry of the finite element system, thus nearly halving the storage requirement and making it ideally suited for solution via a conjugate gradient type of algorithm. Further, the edge-based implementation discussed in [6] requires that the absorbing boundary be placed nearly a wavelength away from the scatterer, whereas in our implementation remarkably accurate results are obtained with the ABCs enforced a small fraction of a wavelength from the scattering body.

2 Formulation

Let us consider the problem of scattering by an inhomogeneous target associated with possible material discontinuities. To solve for the scattered fields via the FEM, it is necessary to enclose the scatterer- embedded inside the volume V- by an artificial surface S_o on which the ABC is enforced (see figure 1). The ABCs to be considered in this paper are the Sommerfeld radiation condition given by

$$\hat{\mathbf{n}} \times \nabla \times \mathbf{E}^s = -jk_o \hat{\mathbf{n}} \times \hat{\mathbf{n}} \times \mathbf{E}^s \tag{1}$$

and the second-order ABC which can be written as

$$\hat{\mathbf{n}} \times \nabla \times \mathbf{E}^s = \alpha \mathbf{E}_t^s + \beta \nabla \times [\hat{\mathbf{n}} (\nabla \times \mathbf{E}^s)_n] + \beta \nabla_t (\nabla \cdot \mathbf{E}_t^s) \tag{2}$$

where $\alpha = jk, \beta = 1/(2jk + 2/r)$, $\mathbf{E}^s$ represents the scattered electric field, $\hat{\mathbf{n}}$ is the unit normal to the surface S_o and the subscripts t and n denote the transverse and normal component to S_o, respectively. When these ABCs are employed on the artificial boundary S_o, they annihilate all field terms of $O(r^{-(2m+1)})$ and smaller, where m denotes the order of the ABC. The ABCs outlined above were derived for spherical surfaces but in this work we have extended their application to S_o which include flat sections. This permits the construction of termination boundaries conformal to the scatterer, thus reducing the size of the the computational domain.

The vector ABCs (1) and (2) can be combined and more conveniently written as

$$\hat{\mathbf{n}} \times \nabla \times \mathbf{E}^s = P(\mathbf{E}^s) \tag{3}$$

for the scattered field formulation in which $\mathbf{E}^s$ is the working variable and

$$\hat{\mathbf{n}} \times \nabla \times \mathbf{E} = P(\mathbf{E}) + \mathbf{U}^{inc} \tag{4}$$

for the total field formulation where the unknown is the total electric field . In (4),

$$\mathbf{U}^{inc} = \hat{\mathbf{n}} \times \nabla \times \mathbf{E}^{inc} - P\left(\mathbf{E}^{inc}\right) \tag{5}$$

where $\mathbf{E} = \mathbf{E}^s + \mathbf{E}^{inc}$ is the total field and $\mathbf{E}^{inc}$ is the incident electric field. Considering (4) to be the boundary condition employed at S_o, we can express the functional for the total electric field as

$$\begin{aligned} F(\mathbf{E}) &= \int_V \left[\frac{1}{\mu_r}(\nabla \times \mathbf{E}) \cdot (\nabla \times \mathbf{E}) - k_o^2 \epsilon_r \mathbf{E} \cdot \mathbf{E}\right] dV \\ &\quad + \int_{S_o} \left[\mathbf{E} \cdot P(\mathbf{E}) + 2\mathbf{E} \cdot \mathbf{U}^{inc}\right] dS \end{aligned} \tag{6}$$

where ϵ_r and μ_r are the relative permittivity and permeability, respectively.

The above functional can be generalized to account for the presence of impedance and resistive sheets or other dicontinuous boundaries. In the case of a resistive card, the transition condition[7]

$$\hat{\mathbf{n}} \times (\hat{\mathbf{n}} \times \mathbf{E}) = -R\hat{\mathbf{n}} \times \left(\mathbf{H}^+ - \mathbf{H}^-\right) \tag{7}$$

must be enforced, where $\mathbf{H}^{\pm}$ denotes the total magnetic field above and below the sheet, R is the resistivity in Ohms per square and $\hat{\mathbf{n}}$ is the unit normal to the sheet pointing in the upward direction (+ side). For an impenetrable impedance surface, the appropriate boundary condition on that surface is

$$\hat{\mathbf{n}} \times (\hat{\mathbf{n}} \times \mathbf{E}) = -\eta \hat{\mathbf{n}} \times \mathbf{H} \tag{8}$$

where $\hat{\mathbf{n}}$ is the unit normal to the surface and η is the surface impedance. Taking into consideration these boundary/transition conditions, the functional for the total electric field can be more explicitly written as

$$\begin{aligned} F(\mathbf{E}) &= \int_V \left[\frac{1}{\mu_r}(\nabla \times \mathbf{E}) \cdot (\nabla \times \mathbf{E}) - k_o^2 \epsilon_r \mathbf{E} \cdot \mathbf{E}\right] dV \\ &\quad + jk_o Z_o \int_{S_k} \frac{1}{K} (\hat{\mathbf{n}} \times \mathbf{E}) \cdot (\hat{\mathbf{n}} \times \mathbf{E})\, dS \\ &\quad + \int_{S_o} \left[\mathbf{E} \cdot P(\mathbf{E}) + 2\mathbf{E} \cdot \mathbf{U}^{inc}\right] dS \end{aligned} \tag{9}$$

where K is the surface resistivity(R) when integrating over a resistive card and equals the surface impedance(η) for an impedance sheet.

The formulation presented above is in terms of the total field but we can easily revert to a scattered field formulation by setting $\mathbf{E}^s = \mathbf{E} - \mathbf{E}^{inc}$ and noting that the scattered field satisfies the wave equation inside the domain of interest. The functional $F(\mathbf{E}^s)$ is given by

$$F(\mathbf{E}^s) = \int_V \left[\frac{1}{\mu_r}(\nabla \times \mathbf{E}^s) \cdot (\nabla \times \mathbf{E}^s) - k_o^2 \epsilon_r \mathbf{E}^s \cdot \mathbf{E}^s\right] dV$$

$$
\begin{aligned}
&+jk_oZ_o\int_{S_k}\frac{1}{K}(\hat{\mathbf{n}}\times\mathbf{E}^s)\cdot(\hat{\mathbf{n}}\times\mathbf{E}^s)\,dS\\
&+\int_{S_o}\mathbf{E}^s\cdot P(\mathbf{E}^s)dS\\
&+2jk_oZ_o\int_{S_d}\frac{1}{\mu_r}\mathbf{E}^s\cdot\left(\hat{\mathbf{n}}\times\mathbf{H}^{inc}\right)dS\\
&+2\int_{V_d}\left[\frac{1}{\mu_r}(\nabla\times\mathbf{E}^s)\cdot(\nabla\times\mathbf{E}^{inc})-k_o^2\epsilon_r\mathbf{E}^s\cdot\mathbf{E}^{inc}\right]dV\\
&+2jk_oZ_o\int_{S_k}\frac{1}{K}(\hat{\mathbf{n}}\times\mathbf{E}^s)\cdot(\hat{\mathbf{n}}\times\mathbf{E}^{inc})dS\\
&+f\left(\mathbf{E}^{inc}\right)
\end{aligned}
\tag{10}
$$

where V_d is the volume occupied by the dielectric (portion of V where ϵ_r or μ_r are not unity), S_d encompasses all dielectric interface surfaces and

$$
\int_{S_o}\mathbf{E}^s\cdot P(\mathbf{E}^s)dS \;=\; \int_{S_o}\left[\alpha\left(\mathbf{E}_t^s\right)^2+\beta(\nabla\times\mathbf{E}^s)_n^2-\beta(\nabla\cdot\mathbf{E}_t^s)^2\right]dS
$$

when the second order ABC is employed. The function $f\left(\mathbf{E}^{inc}\right)$ is solely in terms of the incident electric field and vanishes when we take the first variation of $F(\mathbf{E}^s)$. We remark that the scattered field formulation was implemented in our code; however, we expect that the total field formulation would yield comparable results.

3 Finite element discretization

To discretize the functional given in (10), the volume V is subdivided into a number of small tetrahedra, each occupying the volume V^e ($e=1,2,\cdots,M$), where M denotes the total number of tetrahedral elements. Within each element, the scattered electric field is expressed as

$$
\mathbf{E}^e=\sum_{j=1}^{m}E_j^e\mathbf{W}_j^e=\{\mathbf{W}^e\}^T\{E^e\}=\{E^e\}^T\{\mathbf{W}^e\} \tag{11}
$$

where $\mathbf{W}_j^e$ are the edge-based vector basis functions[4], E_j^e denote the expansion coefficients of the basis and represent the field components tangential to the jth edge of the eth element, m is the number of edges making up the element and the superscript stands for the element number. The basis functions used in our implementation have zero divergence and constant curl.

The system of equations to be solved for E_j^e is obtained by a Rayleigh-Ritz procedure which amounts to differentiating F with respect to each edge field and then setting it to zero. On substituting (11) into (10), taking the first variation in F and assembling all M elements, we obtain the following augmented system of equations

$$
\left\{\frac{\partial F}{\partial E^e}\right\}=\sum_{e=1}^{M}[A^e]\{E^e\}+\sum_{s=1}^{M_s}[B^s]\{E^s\}+\sum_{p=1}^{M_p}\{C^p\}=0 \tag{12}
$$

In this, M_s denotes the number of triangular surface elements on S_k and S_o and M_p is equal to the sum of the surface elements on S_k, S_d and the volume elements in V_d. The elements of the matrices $[A^e]$, $[B^s]$ and $\{C^p\}$ are given by

$$
\begin{aligned}
A^e_{ij} &= \int_{V^e} \left[\frac{1}{\mu_r} (\nabla \times \mathbf{W}^e_i) \cdot (\nabla \times \mathbf{W}^e_j) - k_o^2 \epsilon_r \mathbf{W}^e_i \cdot \mathbf{W}^e_j \right] dV \\
B^s_{ij} &= jk_o Z_o \left[\int_{S^s_k} \frac{1}{K} (\hat{\mathbf{n}} \times \mathbf{W}^s_i) \cdot (\hat{\mathbf{n}} \times \mathbf{W}^s_j) dS \right] \\
&\quad + \int_{S^s_o} \left[\alpha \mathbf{W}^s_{it} \cdot \mathbf{W}^s_{jt} + \beta (\nabla \times \mathbf{W}^s_i)_n \cdot (\nabla \times \mathbf{W}^s_j)_n - \beta (\nabla \cdot \mathbf{W}^s_{it})(\nabla \cdot \mathbf{W}^s_{jt}) \right] dS \\
C^p_i &= 2jk_o Z_o \left[\int_{S^p_d} \frac{1}{\mu_r} \mathbf{W}^p_i \cdot \left(\hat{\mathbf{n}} \times \mathbf{H}^{inc} \right) dS + \int_{S^p_k} \frac{1}{K} (\hat{\mathbf{n}} \times \mathbf{W}^p_i) \cdot (\hat{\mathbf{n}} \times \mathbf{E}^{inc}) dS \right] \\
&\quad + 2 \int_{V^p_d} \left[\frac{1}{\mu_r} (\nabla \times \mathbf{W}^p_i) \cdot (\nabla \times \mathbf{E}^{inc}) - k_o^2 \epsilon_r \mathbf{W}^p_i \cdot \mathbf{E}^{inc} \right] dV
\end{aligned}
$$

where V^p_d is the volume of the pth tetrahedron inside the dielectric, S^s and S^p represent the surface area of the sth and pth triangular surface element and the subscripts t and n denote the tangential and normal components of a vector, respectively. The boundary condition $\hat{\mathbf{n}} \times \mathbf{E}^s = -\hat{\mathbf{n}} \times \mathbf{E}^{inc}$ must be imposed a priori on metallic boundaries; however, no special treatment is required at material discontinuities. Only the identification of the edges on material discontinuities or inhomogeneities is required to kick in the contribution from the surface integrals in (10).

The biconjugate gradient algorithm was used to solve the sparse, symmetric system of equations. The residual norm was usually set to less than 0.1% of the solution norm as a criterion for convergence since lower tolerances did not appear to offer significant improvement on the far-field values. The data structure was constructed such that only the non-zero elements of the upper triangular part of the symmetric, sparse matrix were stored in a $N_a \times k$ complex array. In our case, N_a was typically $1.1 \times N_u$, where N_u denotes the number of unknowns and k was equal to 12. The corresponding addresses were stored in a separate $N_a \times k$ integer array. The storage required in this scheme was about $25N_u$ and the number of distinct non-zero elements was typically $9N_u$.

4 Results

A computer program was written for implementing the proposed FE-ABC formulation. This implementation was validated by computing the scattering for several configurations including metallic and dielectric bodies as well as structures satisfying resistive and impedance boundary conditions.

Figure 2 compares the measured[8] bistatic cross-section ($\theta^{inc} = 180^0$, $\phi^{inc} = 90^0$) of a metallic cube having an edge length of 0.755λ with the corresponding pattern computed by the three-dimensional FE-ABC code.

The second-order vector ABC was employed on a spherical mesh truncation boundary which was placed only 0.1λ from the edge of the cube. About 33,000 unknowns were used for the discretization of the computational domain and the $[A]$ matrix contained a total of 264,000 distinct non-zero entries. The storage requirement of this matrix was consequently much smaller than that of the 1400 unknown moment method system (assuming the same sampling rate as the FEM of 14 points/λ) which had 2 million non-zero entries.

In figure 3, we plot the normal incidence backscatter RCS of a perfectly conducting cube as a function of its edge length. The meshes constructed for this experiment were terminated on conformal boundaries, i.e, on another cube placed a small distance (more than 0.15λ) from the scatterer. As seen, the agreement with measured data[9] is remarkably good over a 50dB dynamic range.

Figure 4 presents backscatter data for a cylinder of radius 0.3λ and height 0.6λ. The data from the three-dimensional finite element code again compare well with that obtained from a moment method-body of revolution code. The mesh was terminated on a spherical boundary at a distance of 0.3λ from the edge of the scatterer and the system consisted of nearly 33,000 unknowns. Convergence was achieved within about 350 iterations when the Sommerfeld radiation condition was imposed on the spherical mesh termination boundary. Each iteration took approximately 0.3 seconds on a Cray YMP and on the average it was found that for $N > 25,000$, the number of required iterations were approximately $N/100$. The agreement was quite good even on enclosing the metallic cylinder in figure 3 with a rectangular outer boundary placed 0.3λ from the edge of the scatterer.

The results presented till now have been for perfectly conducting geometries. However, the real advantage of the FEM over integral equation techniques is the ease with which the former can handle material inhomogeneities and transition conditions. With this in mind, the remaining figures show backscatter and bistatic patterns for scatterers comprised of resistive cards, dielectric material and combinations of these. One of the test cases was a prolate spheroid shown in figure 5 filled with lossy dielectric having a permittivity of $4 - j1$, $k_o a = \pi/2$ and $a/b = 2$, where a and b are the major and minor axes of the spheroid, respectively. The bistatic pattern ($\theta^{inc} = 180°$; $\phi^{inc} = 90°$) obtained from the FE-ABC solution agree reasonably well with those obtained via the hybrid finite element-boundary integral method presented in [2]. However, the corresponding convergence rate for non-metallic bodies and resistive/impedance sheets was found to be slower than that observed for metallic scatterers. A diagonal preconditioner was, therefore, used to accelerate the convergence of the biconjugate gradient algorithm with encouraging results.

For our last example, we compute the scattering from an inhomogeneous geometry with embedded resistive cards. Particularly, the scatterer shown in figure 6 consists of an air-filled resistive card block ($0.5\lambda \times 0.5\lambda \times 0.25\lambda$) joined to a metallic block ($0.5\lambda \times 0.5\lambda \times 0.25\lambda$). In figure 7, we compare a principal plane backscatter pattern obtained from our 3D FE-ABC implementation

with data computed using a traditional moment method code[10]. For the FE-ABC solution, the scatterer was enclosed within a cubical outer boundary placed only 0.3λ away from the scatterer. This resulted in a 30,000 unknown system which converged to the solution in about 400 iterations when using the Sommerfeld radiation condition and in 1600 iterations when the second order ABC was used. For this geometry, the second order ABC did not provide a significant improvement in accuracy (only about 0.1dB) over the first order condition. The same case was run with a higher discretization resulting in a system of 50,000 unknowns; however, there was no significant difference in the far-field values with the earlier case. The geometry for the backscatter pattern shown in figure 8 is the same as in figure 6 with the air-filled section now occupied by a lossy dielectric having $\epsilon_r = 2 - j2$. The backscatter echo-area pattern for the $\phi\phi$ polarization as computed by our FE-ABC code is again seen to be in good agreement with corresponding moment method data[10].

5 Conclusions

In this paper, we have shown that the finite element technique with vector basis functions, when coupled with ABCs for mesh termination and the bi-conjugate gradient algorithm for the solution of the resulting system, is a viable procedure for computing the scattering by three-dimensional targets. We have found that these ABCs can be enforced only a small fraction of a wavelength from the scatterer's surface. This is probably due to the fast $(1/r)$ decay of the scattered fields. As a result, in addition to the sparsity of the matrix, the total number of unknowns is kept under control. Further, due to the use of edge elements, the program can easily handle sharp conducting edges and tips, inhomogeneous dielectric and/or magnetic materials, resistive sheets and impedance surfaces. These, in conjunction with the well-known advantages of the finite element method, results in low $O(N)$ storage requirement, making the computation of large body scattering possible. These capabilities along with the ease in modelling arbitrary geometries, makes this formulation, to the best of our knowledge, one of the first suitable for solving practical three-dimensional scattering problems.

6 Appendix

6.1 Anisotropic case

In order to deal with anisotropic scatterers, the functional outlined in (9) undergoes a slight modification since the material properties of the scatterer (permeability and permittivity) are now second rank tensors rather than scalars. Equation (9) can therefore be written as

$$F(\mathbf{E}) = \int_V \left[(\nabla \times \mathbf{E}) \cdot \left\{ [\overline{\overline{\mu_r}}]^{-1} \cdot (\nabla \times \mathbf{E}) \right\} - k_o^2 \mathbf{E} \cdot \{ \overline{\overline{\epsilon_r}} \cdot \mathbf{E} \} \right] dV$$

$$+jk_oZ_o\int_{S_k}\frac{1}{K}(\hat{\mathbf{n}}\times\mathbf{E})\cdot(\hat{\mathbf{n}}\times\mathbf{E})\,dS$$
$$+\int_{S_o}\left[\mathbf{E}\cdot P(\mathbf{E})+2\mathbf{E}\cdot\mathbf{U}^{inc}\right]dS \tag{13}$$

where

$$\overline{\overline{\mu_r}}=\begin{bmatrix}\mu_{xx} & \mu_{xy} & \mu_{xz}\\ \mu_{yx} & \mu_{yy} & \mu_{yz}\\ \mu_{zx} & \mu_{zy} & \mu_{zz}\end{bmatrix} \tag{14}$$

and

$$\overline{\overline{\epsilon_r}}=\begin{bmatrix}\epsilon_{xx} & \epsilon_{xy} & \epsilon_{xz}\\ \epsilon_{yx} & \epsilon_{yy} & \epsilon_{yz}\\ \epsilon_{zx} & \epsilon_{zy} & \epsilon_{zz}\end{bmatrix} \tag{15}$$

The changes in the scattered field functional (10) and in the elements of the matrices $[A^e]$, $[B^s]$ and $\{C^p\}$ can also be easily incorporated by replacing

$$\frac{1}{\mu_r}\mathbf{X}\cdot\mathbf{Y} \qquad \text{with} \qquad \mathbf{X}\cdot[\overline{\overline{\mu_r}}]^{-1}\cdot\mathbf{Y}$$

and

$$\epsilon_r\mathbf{X}\cdot\mathbf{Y} \qquad \text{with} \qquad \mathbf{X}\cdot\overline{\overline{\epsilon_r}}\cdot\mathbf{Y}$$

where $\mathbf{X}$ and $\mathbf{Y}$ are arbitrary vectors.

7 References

1. J.M. Jin and J.L. Volakis, "Electromagnetic scattering by and transmission through a three-dimensional slot in a thick conducting plane", *IEEE Trans. Antennas Propagat.*, vol. 39, no. 4, pp. 543-550, April 1991.

2. X. Yuan, "Three-dimensional electromagnetic scattering from inhomogeneous objects by the hybrid moment and finite element method", *IEEE Trans. Microwave Theory Tech.*, vol. 38, no.8, pp. 1053-1059, Aug. 1990.

3. I.D. Mayergoyz and J. D'Angelo, "New finite element formulation for 3-D scattering problems", *IEEE Trans. Magnetics*, vol. 27, no. 5, pp. 3967-3970, September 1991.

4. M.L. Barton and Z.J. Cendes, "New vector finite elements for three-dimensional magnetic field computation", *J. Appl. Phys.*, vol. 61, no. 8, pp.3919-3921, April 1987.

5. J.P. Webb and V.N. Kanellopoulos, "Absorbing boundary conditions for finite element solution of the vector wave equation",*Microwave and Opt. Tech. Letters*, vol. 2, no. 10, pp. 370-372, October 1989.

6. J. D'Angelo and I.D. Mayergoyz, "Finite element methods for the solution of RF radiation and scattering problems", *Electromagnetics*, vol. 10, pp. 177-199, 1990.

7. T.B.A. Senior, "Combined resistive and conducting sheets", *IEEE Trans. Antennas Propagat.*, vol. 33, pp. 577-579, 1985.
8. R.P. Penno, G.A. Thiele and K.M. Pasala, "Scattering from a perfectly conducting cube",*Proc. IEEE*, vol. 77, no. 5, pp. 815-823, May 1989.
9. M.F. Catedra, E. Gago and L. Nuño, "RCS of three-dimensional bodies of resonant size", *IEEE Trans. Antennas Propagat.*, vol. 37, no. 5, pp. 528-537, May 1989.
10. Courtesy of Northrop Corp., B2 Division, Pico Rivera, CA.

Figure captions

Figure 1: Illustration of a scatterer enclosed by an artificial surface, S_o, on which the absorbing boundary condition is imposed.

Figure 2: Bistatic pattern of a metallic cube having an edge length of 0.755λ. The dotted circles and squares are measured data.

Figure 3: Backscatter RCS at normal incidence for a metallic cube of side a. The dots indicate measured data.

Figure 4: Backscatter pattern of a perfectly conducting cylinder of radius 0.3λ and height 0.6λ. The axis of the cylinder coincides with the z-axis of the cartesian coordinate system. The dotted circles and squares are data obtained from a moment method code.

Figure 5: Bistatic pattern of a lossy prolate spheroid ($\epsilon_r = 4 - j1$; $k_o a = \pi/2$; $a/b = 2$), where a and b are the major and minor axis of the spheroid, respectively. The dotted circles are data computed from a hybrid FEM/MoM solution.

Figure 6: Geometry of a cube (a=b=0.5λ) consisting of a metallic section and an air-filled section, where the latter is bounded by a resistive surface having $R = Z_o$. The outer cube drawn with dashed lines represents the surface on which the ABC was enforced.

Figure 7: RCS patterns in the x-z plane for the geometry in figure 6 with $H_z^{inc} = 0$(solid curve is the FE-ABC pattern; circles are MOM data) and $E_z^{inc} = 0$(dashed curve is the FE-ABC pattern; black dots are MOM data).

Figure 8: RCS pattern in the x-z plane for the geometry in figure 6 with the air-filled section replaced with dielectric having $\epsilon_r = 2 - j2$. The solid curve is the FE-ABC pattern and the black dots are MoM data for the $E_z^{inc} = 0$ polarization.

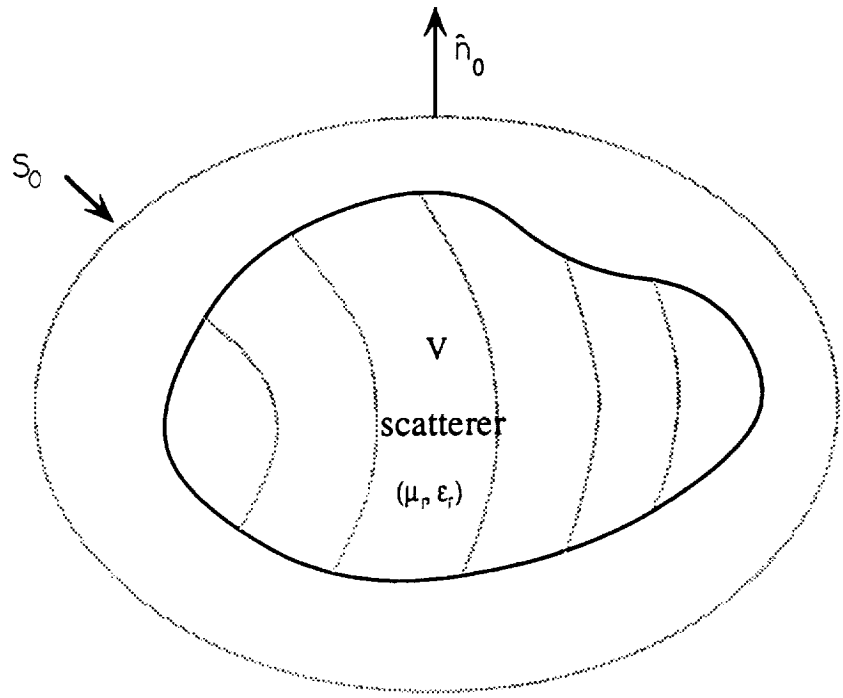

Figure 1. Illustration of a scatterer enclosed by an artificial surface, S_0, on which the absorbing boundary condition is imposed.

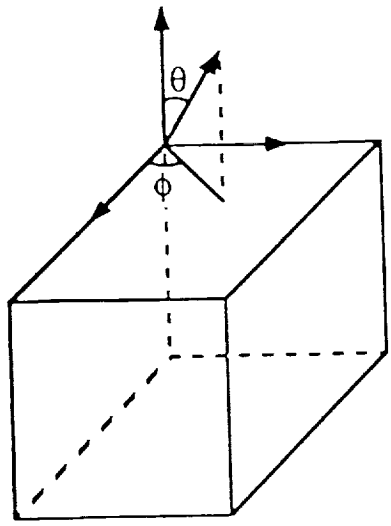

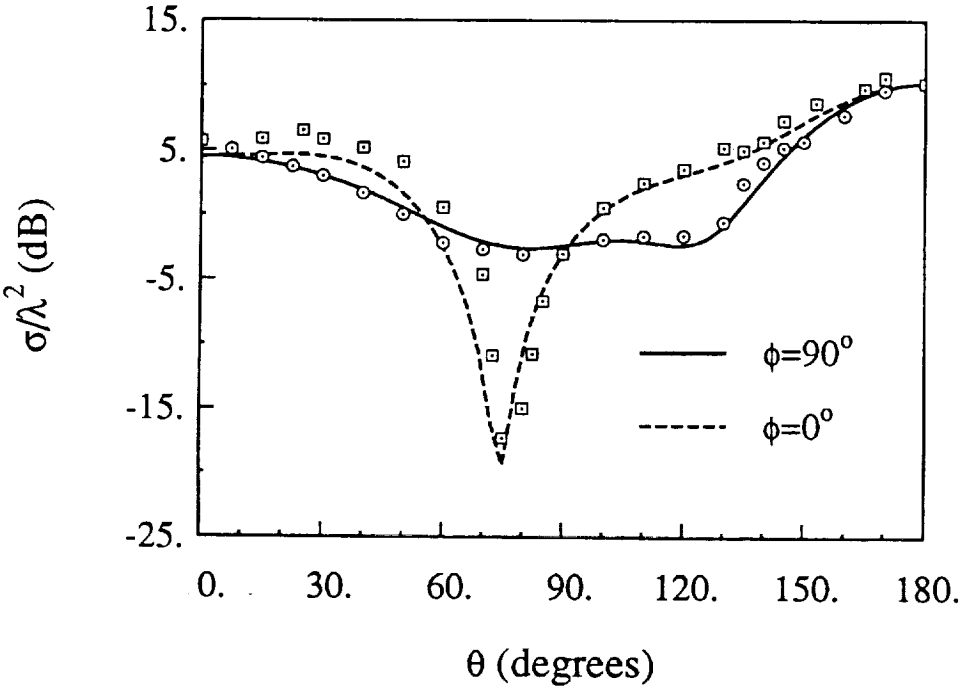

Figure 2: Bistatic pattern of a metallic cube having an edge length of 0.755λ. The dotted circles and squares are measured data.

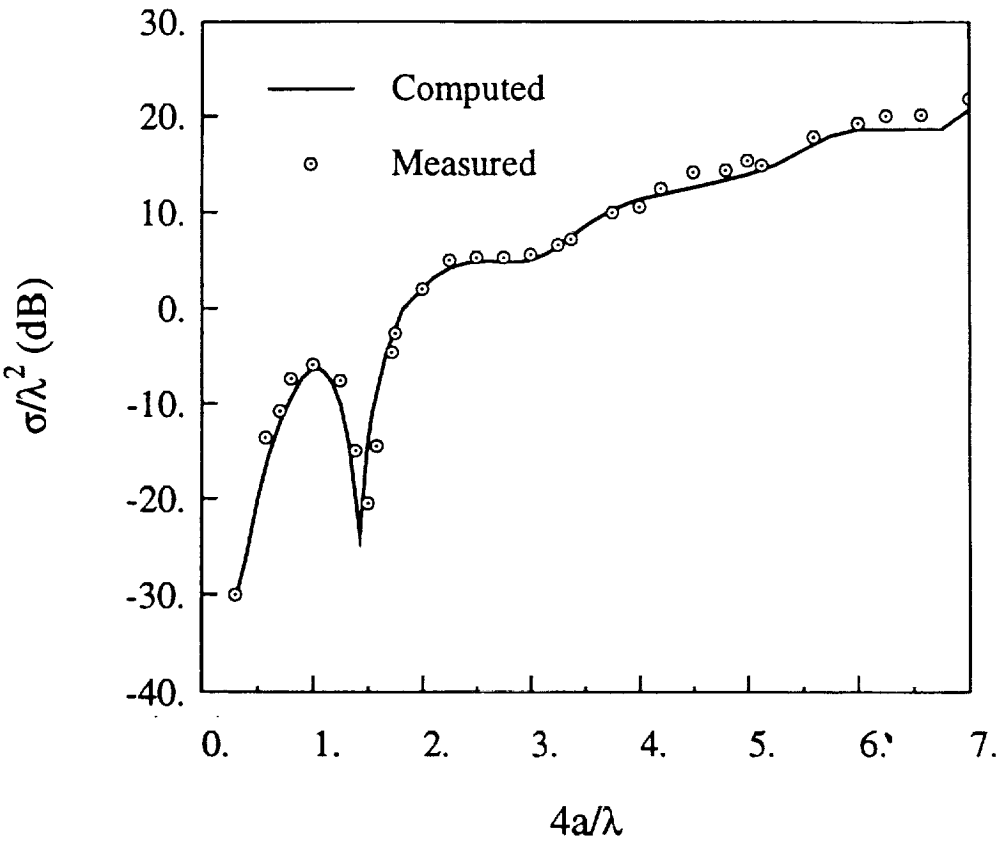

Figure 3: Backscatter RCS at normal incidence of a metallic cube of side a. The dots indicate measured data.

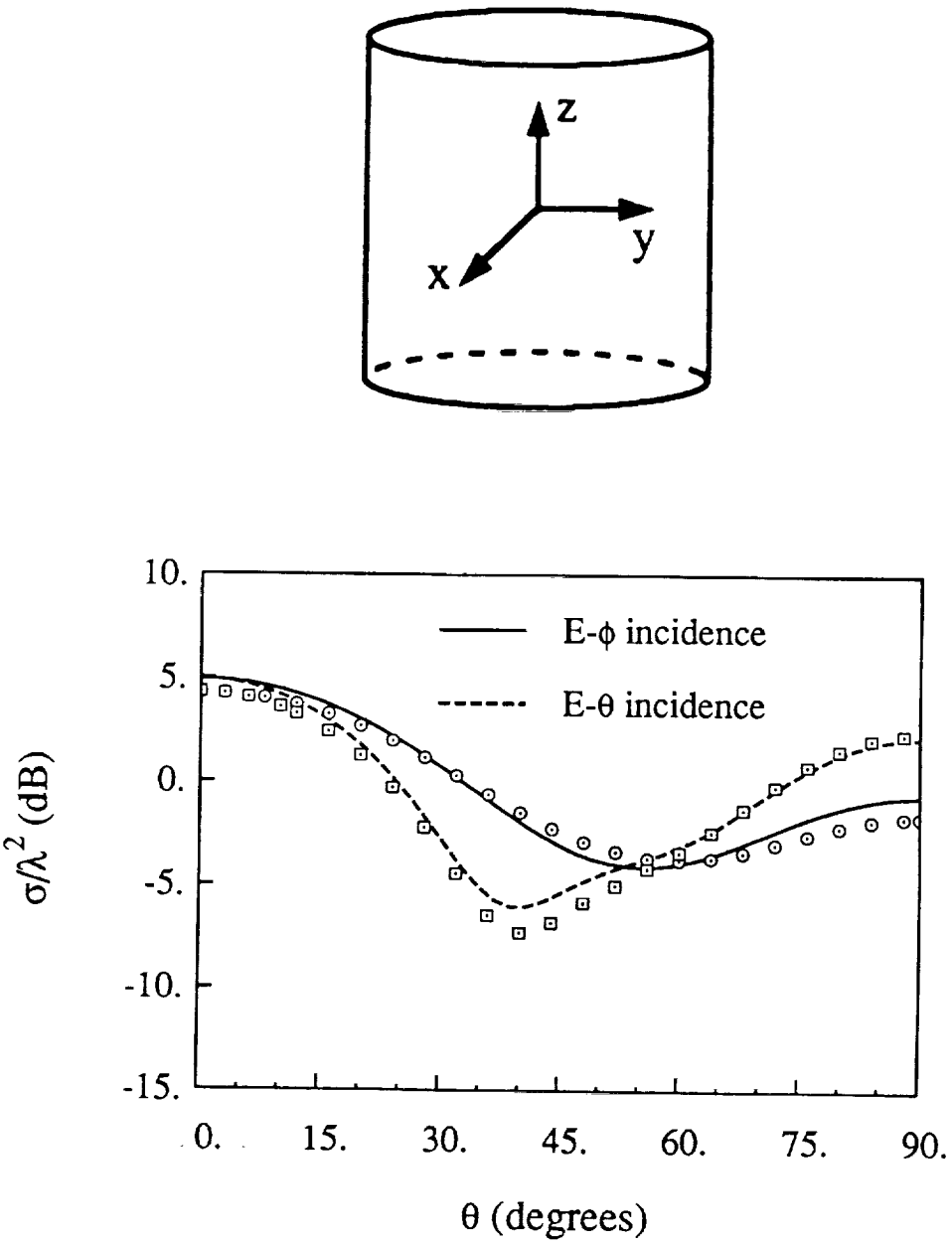

Figure 4: Backscatter pattern of a perfectly conducting cylinder of radius 0.3λ and height 0.6λ. The axis of the cylinder coincides with the z-axis of the cartesian coordinate system. The dotted circles and squares are data obtained from a moment method code.

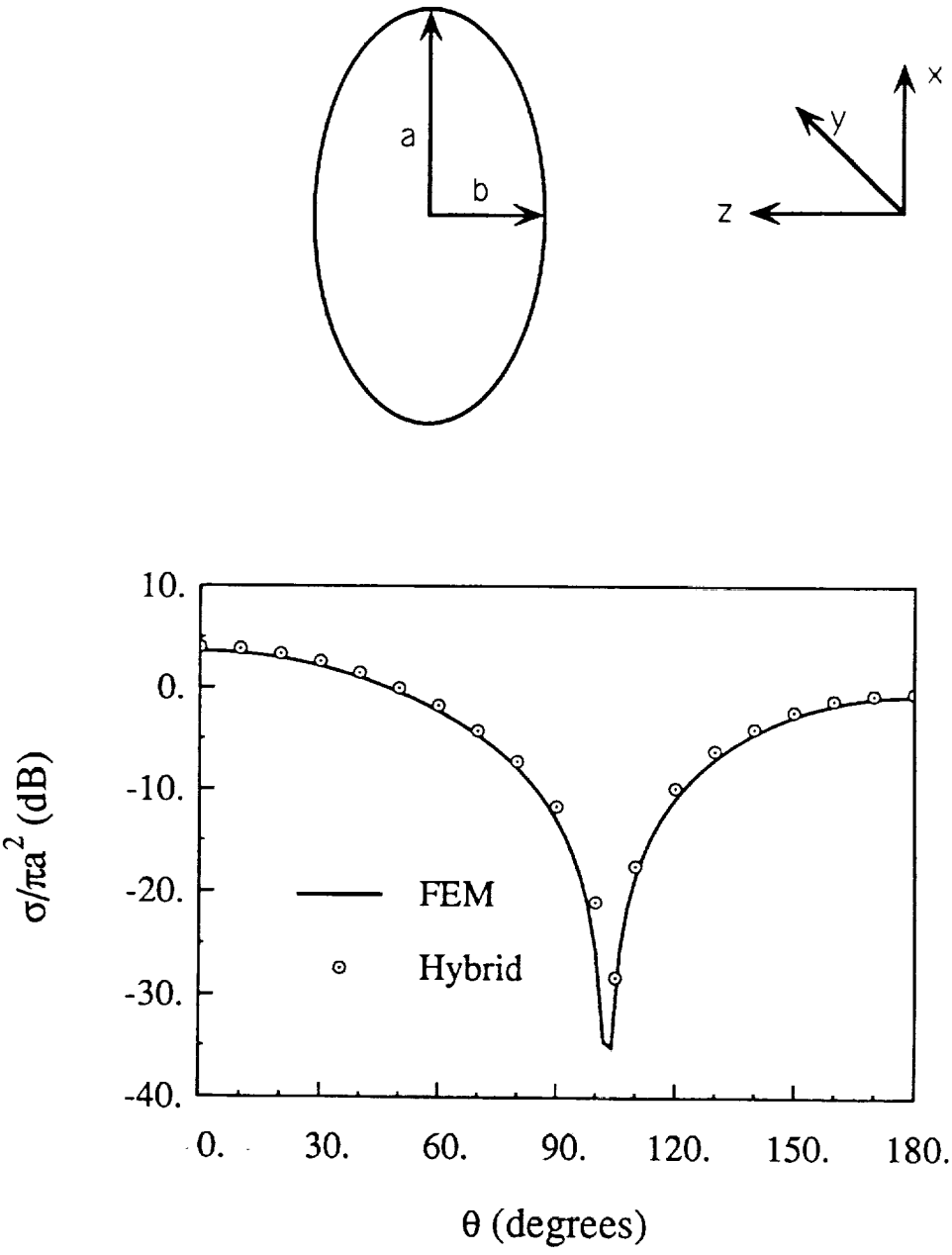

Figure 5: Bistatic pattern of a lossy prolate spheroid ($\epsilon_r = 4 - j1$; $k_o a = \pi/2$; $a/b = 2$), where a and b are the major and minor axis of the spheroid, respectively. The dotted circles are data computed from a hybrid FEM/MoM solution.

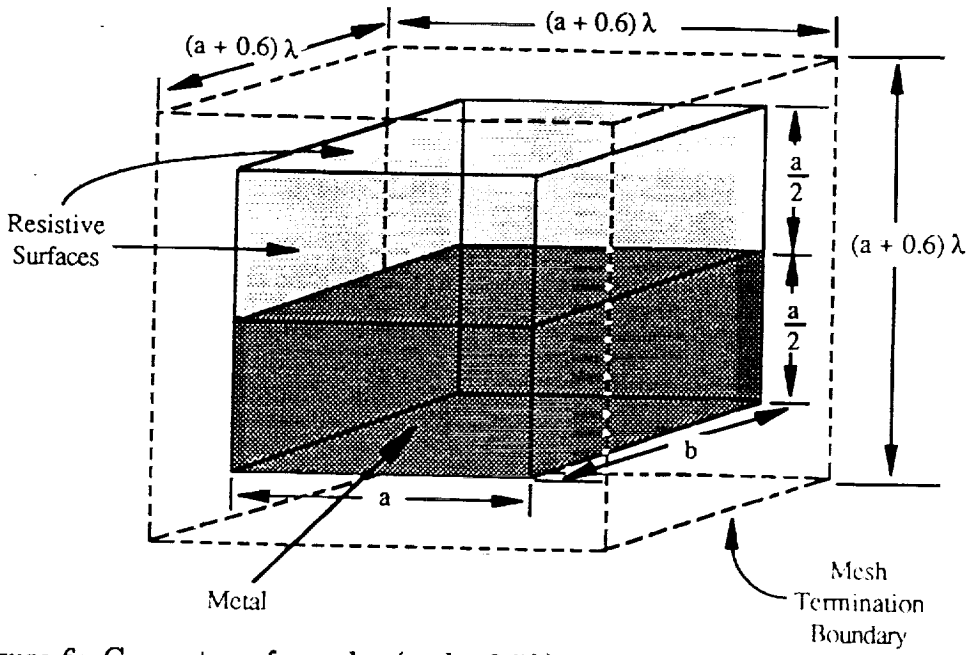

Figure 6: Geometry of a cube (a=b=0.5λ) consisting of a metallic section and an air-filled section, where the latter is bounded by a resistive surface having $R = Z_o$. The outer cube drawn with dashed lines represents the surface on which the ABC was enforced.

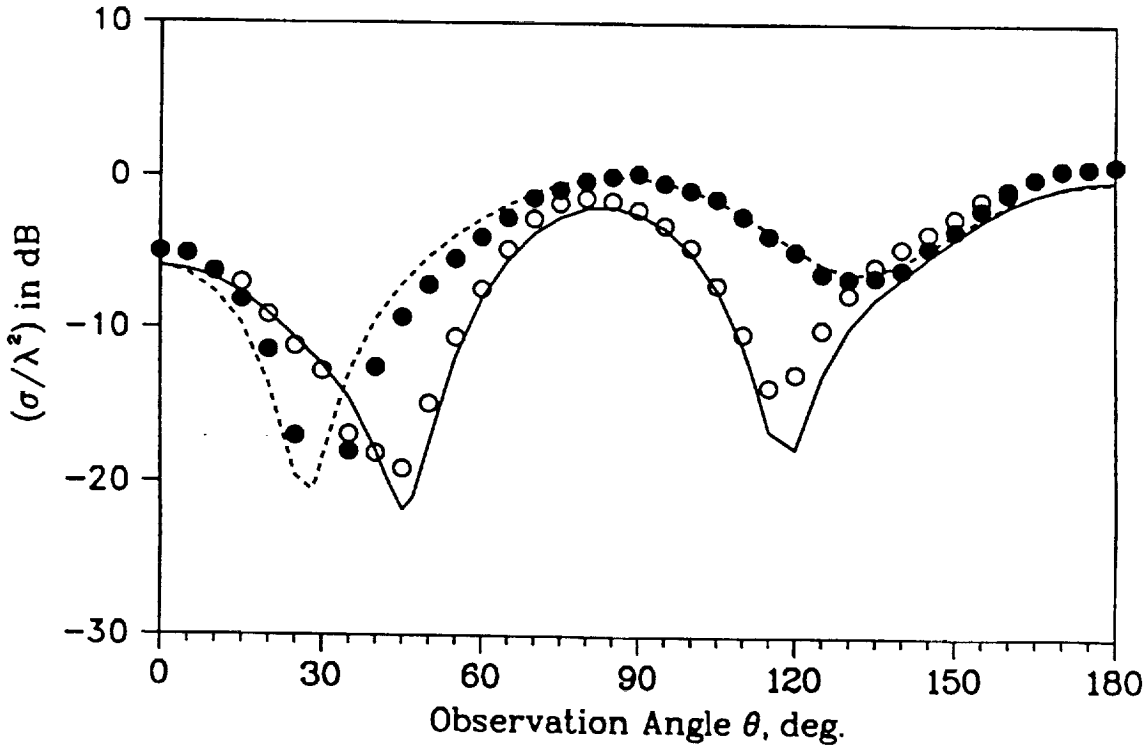

Figure 7: RCS patterns in the x-z plane for the geometry in figure 6 with $H_z^{inc} = 0$(solid curve is the FE-ABC pattern; circles are MOM data) and $E_z^{inc} = 0$(dashed curve is the FE-ABC pattern; black dots are MOM data).

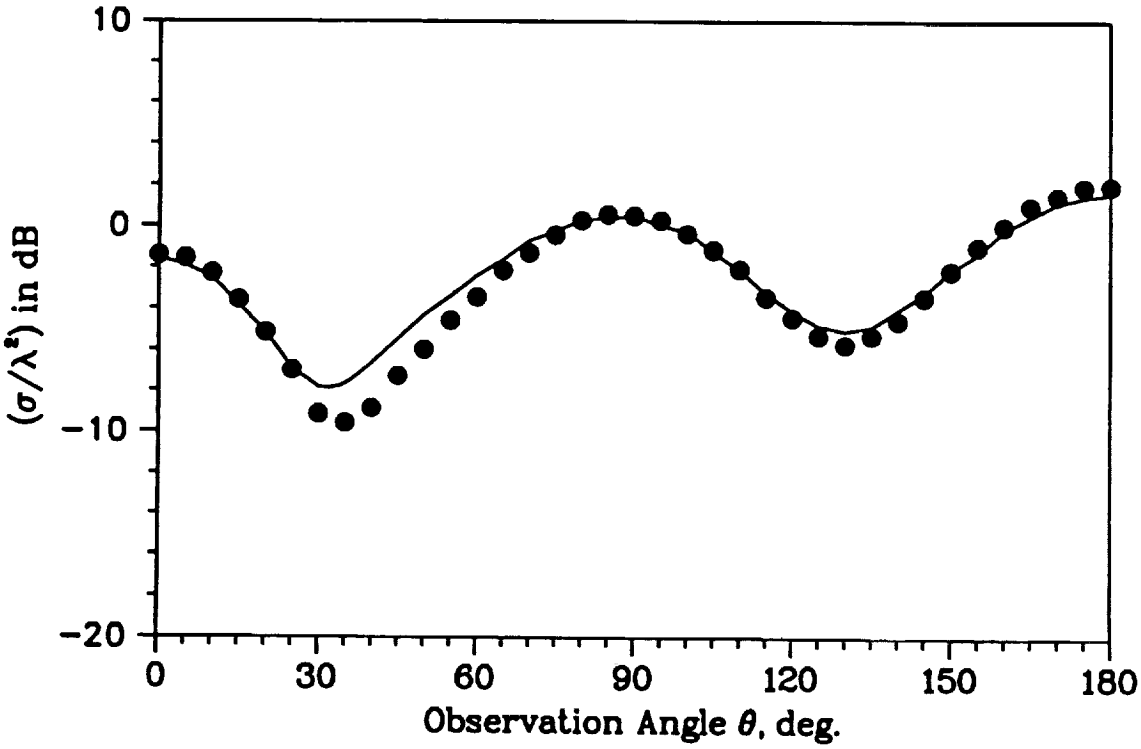

Figure 8: RCS pattern in the x-z plane for the geometry in figure 6 with the air-filled section replaced with dielectric having $\epsilon_r = 2 - j2$. The solid curve is the FE-ABC pattern and the black dots are MoM data for the $E_z^{inc} = 0$ polarization.